Yuan, B. et al. (2023) Dual-wavelength DFB laser array based on sidewall grating and lateral modulation of the grating coupling coefficient. Journal of Lightwave Technology, 41(9), pp. 2775-2784.

https://eprints.gla.ac.uk/289500/

Deposited on: 13 January 2023

Dual-wavelength DFB Laser Array Based on Sidewall Grating and Lateral Modulation of the Grating Coupling Coefficient

Bocheng Yuan, Yizhe Fan, Shengwei Ye, Yunshan Zhang, Yiming Sun, Xiao Sun, Weiqing Cheng, Song Liang, Yongguang Huang, Ruikang Zhang, Jue Wang, John H. Marsh, *Fellow, IEEE*, and Lianping Hou, *Senior Member, IEEE*

Abstract—A monolithic dual-wavelength DFB laser array based on sidewall gratings and a novel modulation of the grating coupling coefficient is proposed and demonstrated experimentally. The grating coupling coefficient distribution along the cavity is modulated by changing the alignment between the gratings on the two sidewalls. The frequency difference between the two lasing modes can be modulated by changing the cavity length and grating recess depth. A series of microwave signals in the range of 50 GHz to 59 GHz is observed after beating the two optical lines in a photodetector. The measured optical linewidths are 250 kHz and 850 kHz when the cavity length is 1200 μm and 1000 μm, respectively.

Index Terms—Monolithic DFB laser, sidewall grating, grating coupling coefficient, microwave generation

I. INTRODUCTION

PHOTONIC generation of microwave signals is attractive for numerous applications, such as spectroscopic sensing, broadband wireless access networks, radar and satellite communications, and has been intensively investigated over the past few years [1]-[5]. The key advantages of photonic techniques for microwave and terahertz generation are the low system cost and flexible tunability, which are difficult to realize using conventional electronics. Normally, the approach for generating microwave wave signals in the optical domain is to beat two optical signals generated by two separate single longitudinal mode (SLM) lasers in a photodetector (PD) [6]-[7]. The beating signal has a frequency equal to the frequency difference between the two optical signals, and the beating signal quality depends on the phase stability of the two SLM lasers. In this approach, a phase tuning section is necessary to improve the coherence of the lasers and the stability of the microwave signal is susceptible to external influences such as temperature and vibration, as these factors can affect the two lasers differently. Applying external modulation to a laser is another method to obtain a microwave signal. A series of optical sidebands will be generated by modulating a laser using

an external modulator. Usually, an optical filter is used to select two optical sidebands. As a result, a high-frequency microwave signal can be optically generated with a low-frequency drive signal, and frequency doubling or quadrupling becomes achievable [8]-[9]. However, this method is complicated since external modulators and optical filters are required.

Compared with the above methods, a monolithic dual-wavelength semiconductor laser (MDSL) is a better way to generate microwave signals. In a MDSL, two optical signals are generated in one physical optical cavity, so external influences have the same effect on the two optical signals. Furthermore, the two signals can be generated by injecting current through a single electrode on the ridge waveguide. The beating signal is generated in a PD without external modulators or optical filters. Introducing two phase shifts in the cavity is an effective way to realize MDSLs [10]-[11]. However, it is difficult to obtain microwave frequencies below 60 GHz by this method in semiconductor DFB lasers since the frequency spacing of the two optical signals is limited by the value of the phase shifts and the chirp rate [11]. MDSLs based on sidewall grating structures can also provide high-quality dual-wavelength lasing and have the potential to be stable terahertz sources [12]. Based on sidewall gratings, the frequency spacing is determined essentially by the grating periods on each sidewall [12]-[13]. Using this method, the minimum resolution of frequency spacing is therefore about 400 GHz, assuming the best resolution of the electron beam lithography (EBL) system used to define the gratings is 0.5 nm and the effective index is 3.2.

In this paper, an array of MDSLs with frequency spacings ranging from 50 GHz to 60 GHz is proposed and demonstrated experimentally. Each MDSL uses a sidewall grating structure and is integrated monolithically with a curved waveguide at the front facet and an electro-absorption modulator (EAM) at the rear facet [14]. The distribution of the grating coupling
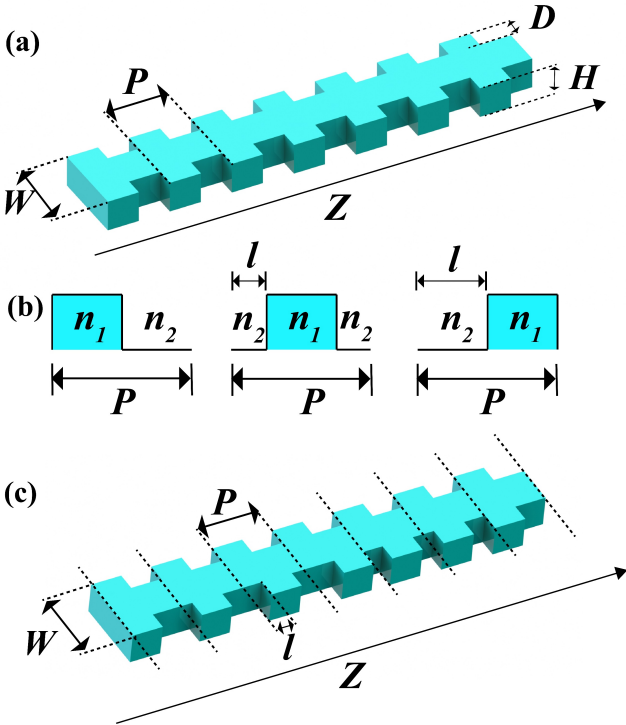
Fig. 1. Schematic of (a) uniform sidewall grating, (b) grating misalignment modulation, and (c) sidewall grating with alignment modulation.

coefficient in the cavity is modulated by controlling the relative alignment of the gratings on either side of the sidewall in each grating period. When the distribution of κ exhibits an inverse-Gaussian curve along the cavity, the side lobes on both sides of the stopband in the transmission spectrum are amplified, thereby forming two transmission peaks, leading to dual-wavelength lasing. The frequency spacing of the two optical signals can be determined by changing the cavity length L and lateral etch recess depth D of the sidewall gratings. To the best of our knowledge, this is the first proposal for applying this grating modulation technique to semiconductor DFB lasers.

II. PRINCIPLE AND SIMULATION RESULTS

In a uniform sidewall grating, the gratings on either side of the sidewall have the same period P, the same lateral etch recess depth D and the corrugations on both sides are completely symmetrical as shown in Fig. 1(a). Each grating period comprises two refractive index segments n_1 and n_2; these are located on the left and right sides of the waveguide and the high index segments on either side are in perfect alignment (Fig. 1(a)).

However, the position of the n_1 segment in each grating period can be changed while keeping the grating period and duty cycle the same. Here, the variable alignment factor l is used to describe the relative positions of the n_1 segment in one grating period (Fig. 1(b)) and its value is the length from the start of the grating period to the start of the n_1 segment.
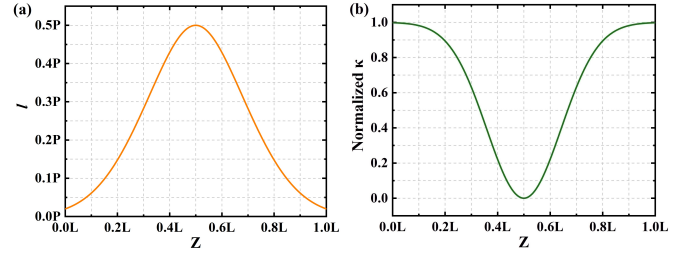

Fig. 2. The distribution of (a) variable alignment factor l and (b) κ along the cavity.

Fig. 1(b) shows schematics of a grating period with $l = 0$, $P/4$ and $P/2$ respectively. In the grating structure proposed here, one sidewall has a uniform Bragg grating and the other sidewall has a grating whose alignment with the uniform grating is modulated along the device. The two gratings have the same period P and 50% duty cycle but on one sidewall l is modulated along the cavity as shown in Fig. 1(c). As l varies along the cavity, the degree of alignment of the gratings on the two sidewalls changes, therefore κ is modulated accordingly [15]. The relationship between κ and the variable alignment factor l can be expressed as [15],

$$\kappa(z) = \kappa_0 \cos\left(\frac{\pi \cdot l(z)}{P}\right) \tag{1}$$

where κ_0 is the grating coupling coefficient when the gratings on both sides have no misalignment (i.e., $l = 0$), and $l(z)$ describes the l distribution along the cavity (i.e., in the z-dimension). Equation (1) shows that the modulation in κ along the cavity can be determined by $l(z)$. If $l(z)$ is designed to be,

$$l(z) = \frac{P}{\pi} \cdot \arccos\left[1 - \exp\left(\frac{-4 \cdot ln2 \cdot (z - L/2)^2}{(L/3)^2}\right)\right] \tag{2}$$

where L is the cavity length, the normalized κ distribution along the cavity is,

$$\kappa(z) = 1 - \exp\left[\frac{-4 \cdot ln2 \cdot (z - L/2)^2}{(L/3)^2}\right] \tag{3}$$

Fig. 2 shows the $l(z)$ and $\kappa(z)$ distribution along the cavity. At the middle of the cavity (i.e., $z = 0.5L$), l reaches a maximum value of $0.5P$, which means the gratings on both sides of the ridge waveguide are completely misaligned and the normalized κ reaches its minimum value.

When κ has an inverse-Gaussian distribution along the cavity as shown in (3), the two sidelobes of the stopband are significantly enhanced and form two transmission peaks which allow dual-wavelength lasing [16]-[17]. The calculated transmission spectra and the time delay spectra based on the transfer matrix method (TMM) are shown in Fig. 3. In the calculations, the effective index n_{eff} is set to 3.19, the grating period P is set to 244 nm, κ_0 is 40/cm, and the cavity length L is 1000 μm. As shown in Fig. 3(a), a uniform grating provides a dominant reflection (stopband) with weak sidelobes on both sides. The peaks in the transmission spectrum between the sidelobes and the stopband are too shallow to support dual-wavelength lasing. With modulation, the sidelobes are significantly enhanced, resulting in two deep and narrow peaks as shown in Fig. 3(b). The time-delay spectrum shown in Fig.3(c) also illustrates that the time-delay peaks of λ_1 and λ_2 are significantly enhanced with the modulation scheme. Since
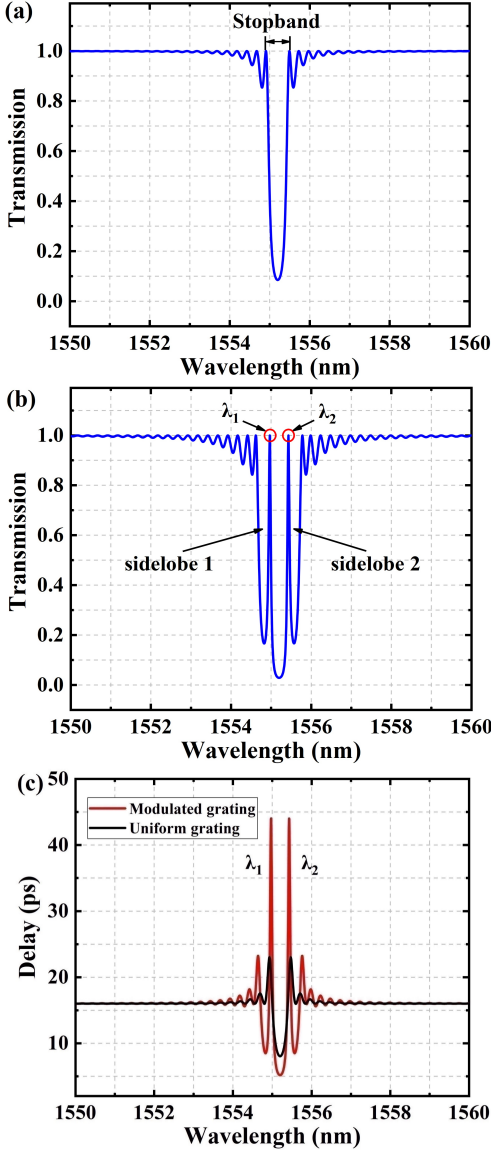
Fig. 3. The simulated transmission spectra of (a) uniform sidewall grating, and (b) sidewall grating with misalignment modulation. (c) The time delay spectrum of sidewall grating with misalignment modulation.

the positions of the lasing wavelengths (λ_1 and λ_2) are the positions of the first zeros on either side of the maximum reflectivity, the wavelength spacing is equal to the width of the stopband which is related to L and κ_0 [18].

Using the TMM, we calculated the wavelength spacing for different L and κ_0. As shown in Fig. 4, the frequency spacing increases with increasing κ_0, and decreases with increasing L. This result is consistent with the change law of the stopband width with κ_0 and L [17], and also indicates that the frequency spacing can be designed through appropriate choices of κ_0 and L.
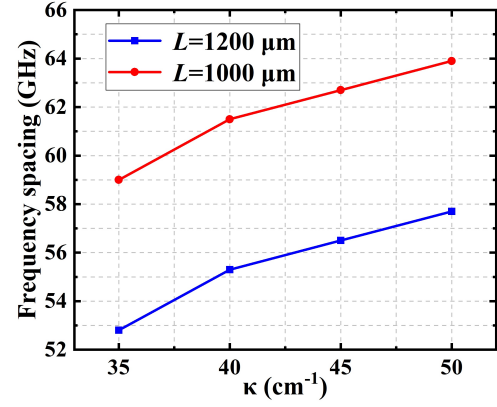

Fig. 4. Frequency spacing between the two lasing modes versus κ_0 under cavity lengths of 1000 μm and 1200 μm.
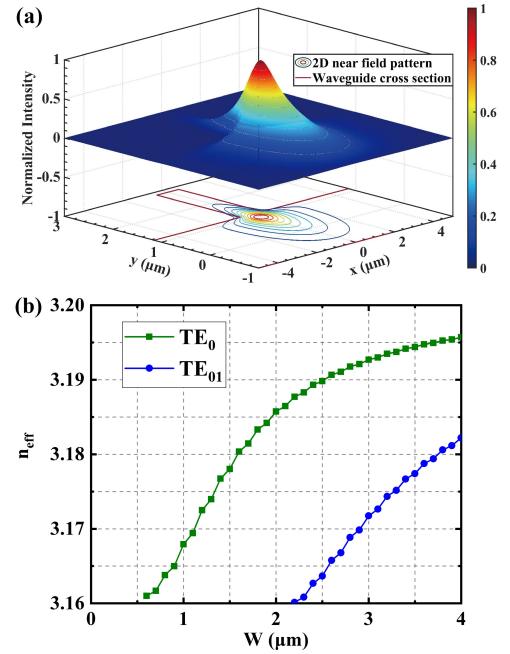
Fig. 5. (a) Simulated near field patterns of the proposed device when $W = 1.12$ μm. (b) Simulated n_{eff} of TE_0 and TE_{01} as a function of W.

According to coupled mode theory, κ_0 can be expressed as [19],

$$\kappa_0 = \frac{\sin(m\pi\gamma)}{m} \frac{(n_1^2 - n_2^2)}{\lambda_B n_{eff}} \Gamma_{x,y} \qquad (4)$$

where λ_B is the Bragg wavelength, and $\Gamma_{x,y}$ is the field overlap integral within the grating region. A first-order grating ($m = 1$) was adopted in our device to facilitate grating fabrication and the duty cycle γ was set to 0.5. n_1 and n_2 are the refractive indexes of the semiconductor and the dielectric material between the etched gratings, respectively. According to Eq. (4), κ_0 is proportional to $\Gamma_{x,y}$, which can be increased by increasing
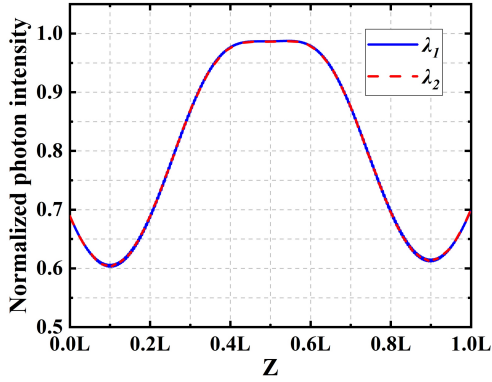
Fig. 6. Photon distributions of λ_1 and λ_2 along the cavity.

the lateral etch recess depth D. The values of κ_0 under different D were calculated and the results are shown in Table. 1. In the calculations, λ_B was set to 1555 nm, n_{eff} was 3.19 and the ridge waveguide width W was 2.5 µm.

TABLE I

CALCULATED κ_0 UNDER DIFFERENT D

D (µm)	κ_0 (cm^{-1})
0.60	89
0.63	94
0.66	99
0.69	103

From the calculations, κ_0 can reach 103 cm^{-1} when D is 0.69 µm. However, due to the reactive ion etching (RIE) lag effect, the actual κ_0 of a fabricated grating is smaller than this value [20]-[21]. Using Lumerical mode solutions, we simulated the near field patterns when W changes from 0.1 µm to 4 µm. As shown in Fig. 5(a), a beam can be confined by a ridge waveguide with a width of 1.12 µm, which is equivalent to a 2.5-µm-wide ridge waveguide minus two 0.69-µm-recess gratings on both sidewalls. In Fig. 5(a), the bottom is a projection of the near-field intensity pattern, and the red line outlines the waveguide cross-section. Fig. 5(b) shows the n_{eff} of the TE$_0$ and TE$_{01}$ modes for different W; the cut-off ridge waveguide width for TE$_0$ is 0.6 µm.

The photon distributions along the cavity for the two lasing modes λ_1 and λ_2 were also calculated. As shown in Fig. 6, the two modes have the same photon distribution, which may lead to the two modes building up a strong correlation [13]. However, the overlap of the two photon distributions may also cause severe mode competition [22]. Therefore, an EAM section is used to adjust the output power and phase of the two lasing modes [14].

III. DEVICE FABRICATION AND CHARACTERISTICS

The epitaxial structure of the device emitting at 1.55 µm is based on an AlGaAsIn-InP heterostructure, grown by metal–organic vapor phase epitaxy (MOVPE). The active layer
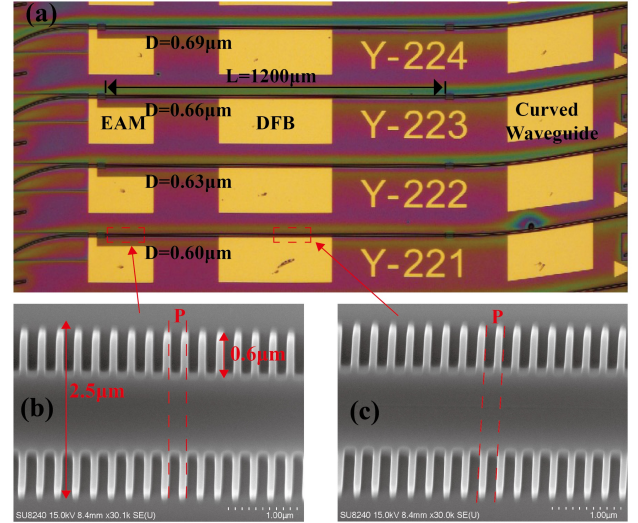

Fig. 7. (a) Microscope image of the dual-wavelength DFB laser array with L=1200 µm, (b) SEM image of the grating at beginning of the DFB cavity, (c) SEM image of the grating at the middle of the DFB cavity.

contains five (6-nm-thick) compressively strained (1.2%) wells and six (10-nm-thick) slightly tensile strained barriers, located in the center of a graded-index, separate-confinement heterostructure (GRINSCH) layer (60 nm on each side) as reported in [23].

The isolation grooves with a depth of 250 nm were first etched by RIE, providing electrical isolation between the DFB, EAM and curved waveguide sections. Then, the first-order gratings with a period of 244 nm and the 2.5-µm-wide ridge waveguide with a height of 1.92 µm were defined by electron beam lithography (EBL) with a resolution of 0.5 nm using hydrogen silsesquioxane (HSQ) resist in a single step. After developing, the resist patterns were transferred to the sample by RIE using Cl$_2$-CH$_4$-H$_2$-Ar etch gases. After the deposition of a further SiO$_2$ layer, a 1.5-µm-wide contact window was opened on top of the ridge waveguide, and p- and n-metal contacts were deposited on both the top highly doped InGaAs contact layer and substrate sides respectively. As a final step, the sample was cleaved into individual laser bars with two facets uncoated.

A microscope image of the dual-wavelength DFB laser array with L=1200 µm is shown in Fig. 7(a). Each device comprises an EAM section (30-µm-long), a DFB section, and two curved waveguides on the rear and front facets with electrical isolation grooves (30-µm-long) between them. The tilts of the curved waveguides at the front and rear facets are 10° and 30° and their radius are 2000 µm and 800 µm, respectively. The curved waveguides reduce the facet reflection, therefore the Fabry-Perot (FP) modes are greatly suppressed. Scanning electron microscope (SEM) images of the HSQ mask patterns at the beginning and the center of the cavity of the DFB section are shown in Fig. 7(b) and (c) respectively. At the beginning of the grating, i.e., at $l = 0$, the gratings on both sidewalls are aligned. At the middle of the grating, $l = P/2$ and the gratings on the sidewalls are antisymmetric.
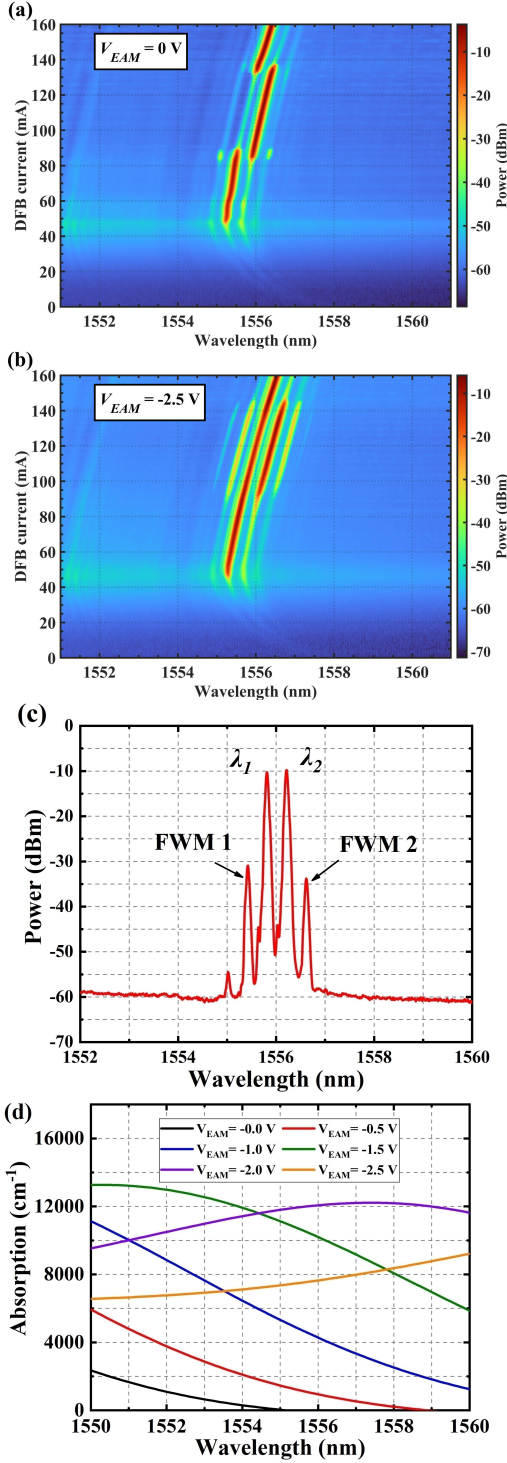
Testing of the devices was carried out under continuous-

Fig. 8. 2-D optical spectrum map of a laser with $L = 1200$ μm, D=0.6 μm when the EAM reverse voltage (V_{EAM}) is (a) 0 V and (b) –2.5 V. (c) Measured optical spectrum when I_{DFB}=100 mA, V_{EAM}= –2.5 V. (d) Simulated absorption spectrum of the EAM under different V_{EAM}.

wave (CW) conditions, with the laser chips mounted on a copper heat sink at 20 °C. The optical outputs were measured from the front facet using an optical spectrum analyzer (OSA) with 0.06 nm resolution bandwidth (RBW) and the injection current in the front curved waveguide was maintained at 30 mA

to reduce material absorption. The optical spectra of a device with $D = 0.6$ μm and $L = 1200$ μm when the DFB injection current (I_{DFB}) changes from 0 mA to 160 mA are shown in Fig. 8.

In Fig. 8(a), it can be seen that good dual wavelength operation occurs only over the limited DFB current range 84 mA – 89 mA. This is because there is severe competition between the two modes λ_1 and λ_2. When one of the modes has a higher gain, the other mode is easily suppressed. The integrated EAM has different absorption coefficients for different wavelengths and the absorption edge will be redshifted with V_{EAM}. Once a suitable V_{EAM} is applied to the EAM, λ_1 and λ_2 will be absorbed to different degrees, thus establishing a new equilibrium state where both λ_1 and λ_2 experience the same gain and therefore emit approximately the same optical power. In addition, the EAM section enhances the coupling between the two lasing modes, improves phase locking and stabilizes the mode beating frequency through the mechanism of nondegenerate four-wave mixing (FWM) based on the carrier-density pulsation (CDP) and spectral-hole burning (SHB) effects [14]. As shown in Fig. 8(b), the device operates in a good dual wavelength lasing condition for DFB currents from 93 mA to 145 mA with –2.5 V applied to the EAM. The current range for the dual wavelength operation condition is significantly improved compared with that for V_{EAM} =0 V (Fig. 8(a)). Fig. 8(c) shows the spectrum when V_{EAM}= –2.5 V and I_{DFB}=100 mA. Two strong FWM signals (FWM 1 and FWM 2) which are enhanced by the EAM can be observed on either side of λ_1 and λ_2. Fig. 8(d) shows the simulated absorption spectrum of the EAM. The results show that under different V_{EAM}, the EAM has different absorption coefficients for λ_1 and λ_2.

TABLE II
THE WAVELENGTH OF THE SIGNALS

Signal	Wavelength
FWM 1	1555.426 nm
λ_1	1555.815 nm
λ_2	1556.215 nm
FWM 2	1556.614 nm

Table II shows the wavelength values of λ_1 ,λ_2 , FWM 1 and FWM 2. Considering that the resolution of our OSA is 0.06 nm, the spacing between any two adjacent signals is 0.4 nm. Fig. 9(a) shows the wavelength spacing between λ_1 and λ_2 ($\Delta\lambda$), and the power margin between λ_1 and λ_2 (PM) for different I_{DFB} when V_{EAM} is –2.5 V. As shown in Fig. 9(a), $\Delta\lambda$ remains equal to 0.4 nm with fluctuations within the OSA RBW when I_{DFB} is increased from 80 mA to 160 mA. The PM is at a low level when I_{DFB} is increased from 100 mA to 150 mA, and overall is less than 4 dBm over this range. The minimum PM is 0.4 dBm when I_{DFB} is 104 mA. The $\Delta\lambda$ under different V_{EAM} is shown in Fig. 9(b). During the measurement, $\Delta\lambda$ was recorded when the PM reached its lowest value for each value of V_{EAM}. The fluctuations in $\Delta\lambda$ are also within the OSA RBW.
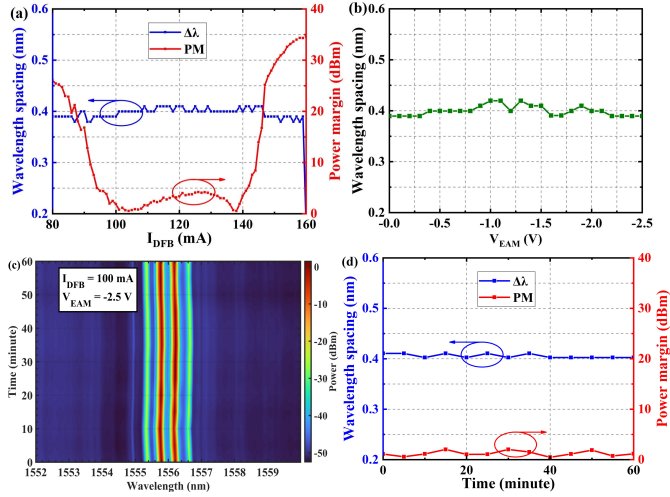
Fig. 9. (a) $\Delta\lambda$ and power margin between λ_1 and λ_2 versus I_{DFB} when V_{EAM} is −2.5 V. (b) $\Delta\lambda$ versus V_{EAM}. (c) One-hour 2-D spectral scan of a laser at time intervals of 5 min when $L=$ 1200 μm, $D=0.6$ μm. (d) $\Delta\lambda$ and power margin between λ_1 and λ_2 versus time.
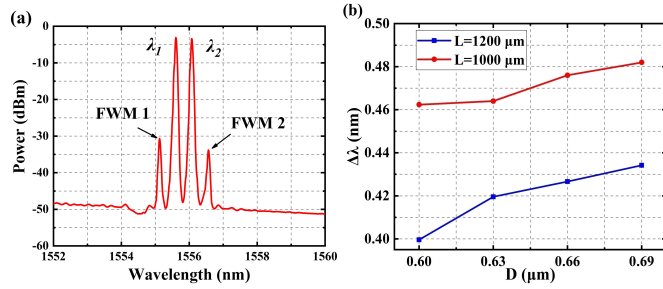

Fig. 10. (a) The optical spectrum of the device with $L=1000$ μm, $D=0.6$ μm when I_{DFB} is 110 mA and V_{EAM} is −1.1 V. (b) $\Delta\lambda$ measured from optical spectra for different L and D values.

A continuous scanning spectrum of the device over a period of 1 hour at 5 min intervals is shown in Fig. 9(c). The small drift of λ_1 and λ_2 is caused by the noise of the DC sources driving the DFB laser and the front curved waveguide, and of the voltage source driving the EAM, and environmental influences such as temperature fluctuations and mechanical vibration. Temperature fluctuations inside the device would be suppressed after the device is packaged. In Fig. 9(d), during the 1-hour measurement, $\Delta\lambda$ remains 0.4 nm with fluctuations within the OSA RBW and the PM remains less than 2.1 dB.

According to the simulation results, changing L and κ_0 will lead to changes in $\Delta\lambda$. A laser array with $L = 1000$ μm and $D=0.60$ μm, 0.63 μm, 0.66 μm, and 0.69 μm has also been fabricated and tested under CW conditions at 20˚C.

As shown in Fig. 10 (a), two main modes (λ_1 and λ_2) and two beating signals (FWM 1 and FWM 2) can be observed. As a result of L being decreased to 1000 μm, $\Delta\lambda$ increases to 0.462 nm. In Fig. 10(b), $\Delta\lambda$ measured from the optical spectra becomes larger as D increases and becomes smaller as L increases. This variation is consistent with the simulated results shown in Table I and Fig. 4.
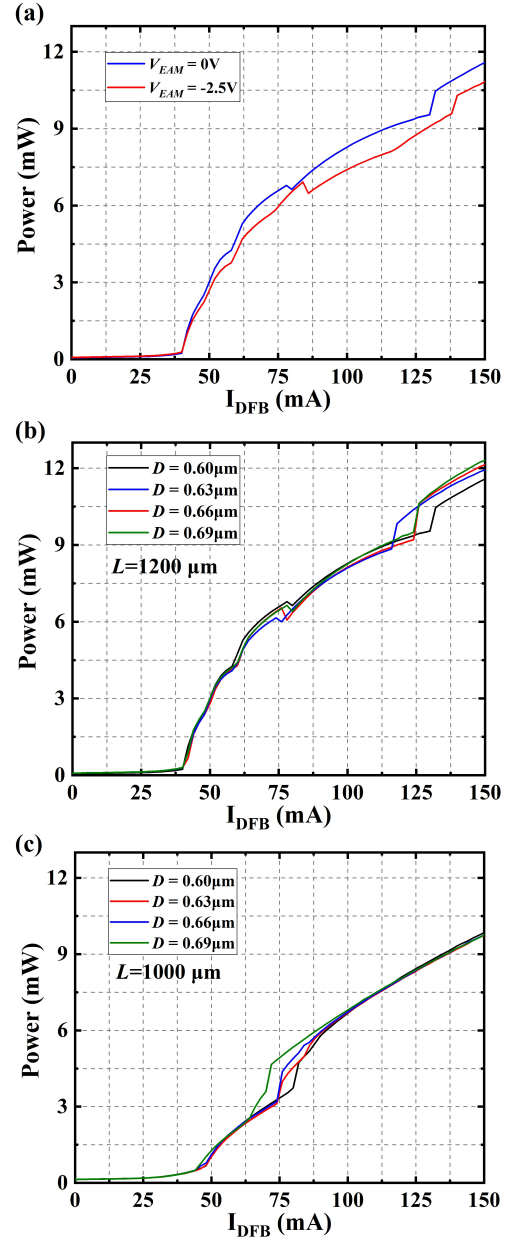

Fig. 11. Measured P-I curves for (a) $L=1200$ μm, $D=0.6$ μm, (b) a laser array with different D values when $L=1200$ μm, $V_{EAM}=0$ V, (c) a laser array with different D values when $L=1000$ μm, $V_{EAM}=0$ V.

Fig. 11 shows the measured power-I_{DFB} (P-I) characteristics from the front facets of the devices with a I_{DFB} scanning step of 2 mA and the injection current in the front curved waveguide kept at 30 mA. As shown in Fig.11(a), the device with $L=1200$ μm has a threshold current of 40 mA. When V_{EAM} is 0 V, there are two discontinuities at 80 mA and 128 mA, which arise because the main lasing mode jumps between λ_1 and λ_2 . The discontinuities are consistent with the results shown in Fig. 8(a). Similarly, when −2.5 V is applied to the EAM, the two discontinuities occur at 86 mA and 144 mA, respectively. When V_{EAM} is increased from 0 V to −2.5 V, the threshold current is unchanged, but the slope efficiency is reduced slightly due to the increased absorption in the EAM. The slope efficiencies are

0.103 W/A and 0.096 W/A when V_{EAM} is 0 V and −2.5 V, respectively. As shown in Fig. 11(b) and (c), a decrease in κL results in an increase in the threshold current to 48 mA when L is reduced from 1200 μm to 1000 μm [24]. Compared to L=1200 μm, there is a lower slope efficiency of 0.09 W/A when L=1000 μm.

The radio frequency (RF) signal was measured using a PD connected to an electrical spectrum analyzer (ESA). The optical signal was coupled by a lensed fiber from the front facet of the device. The fiber was connected to an erbium-doped fiber amplifier (EDFA, Pritel Inc FA-23, optical noise figure <6 dB) via an optical isolator and polarization controller. The optical isolator prevents amplified light from being reflected back to the device through the lensed fiber. The amplified optical signal was converted into an electrical signal by a PD (u2t Photonics XPDV2020R 50 GHz) and then sent to an external mixer (Keysight 11970V) via a coax-to-rectangular waveguide connector. The function of the diplexer is to separate/combine the LO/IF signal for the ESA (Keysight N9020B). The whole system is shown in Fig. 12.

By properly adjusting I_{DFB} and V_{EAM}, a series of stable RF signals from different devices were captured by the ESA within a scanning range of 14 GHz and at a resolution of 50 kHz. the 8 RF signals from 8 devices with different L and D can be observed in Fig. 13(a). The parameters of the RF signals and the operating conditions of the laser arrays are shown in Table III. When L=1200 μm, as D increases, the frequency of the RF signal f increases from 50.04 GHz to 53.71 GHz. As a result of L decreasing to 1000 μm, higher values of f from 57.11 GHz to 59.73 GHz are observed, behavior consistent with the earlier simulations. The device (L=1200 μm, D=0.6 μm) was operated over a period of 1 hour under I_{DFB} =105 mA and V_{EAM}=-2.5 V, and the recorded frequency and RF intensity as a function of time (recorded at 5 min intervals) are shown in Fig. 13(b), (c). During the 1 hour measurement, the RF frequency was 50.04 GHz with a drift of less than 25 MHz. Meanwhile, the RF intensity exhibited a variation of less than 5.5 dBm. The frequency drift is caused by temperature fluctuations inside the device and the intensity variation is due to changes of the PM. This phenomenon would be suppressed by packaging the device.

It should be noted that the V_{EAM} applied to DFB lasers with L=1000 μm is lower (less negative) than that for L=1200 μm. This is because the 1000-μm-long DFB lasers have lower output powers than for L=1200 μm, and saturation of the absorption can be achieved at a lower V_{EAM}.

It should also be noted that during the measurement, I_{DFB} of different devices with same L has a maximum spread of 11 mA. The larger I_{DFB} will give a larger red shift to λ_1 and λ_2, thus resulting in a frequency shift of the RF signal. The results shown in Fig. 9 illustrate that $\Delta\lambda$ remains the same as I_{DFB} and V_{EAM} are changed. Therefore, the frequency versus different wavelength center of λ_1 and λ_2 can be calculated from (5)

$$f_s = \frac{c \cdot \Delta\lambda}{(\lambda_c + 0.5\Delta\lambda)(\lambda_c - 0.5\Delta\lambda)} \quad (5)$$

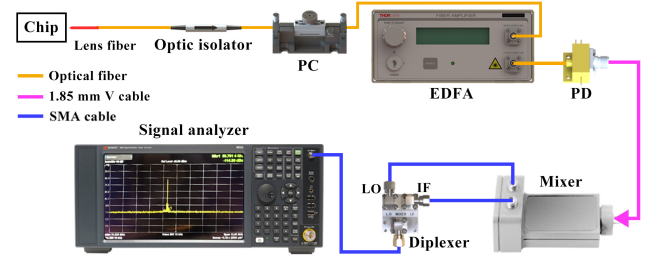where f_s is the calculated frequency, $\Delta\lambda$ is kept at 0.4 nm, λ_c is

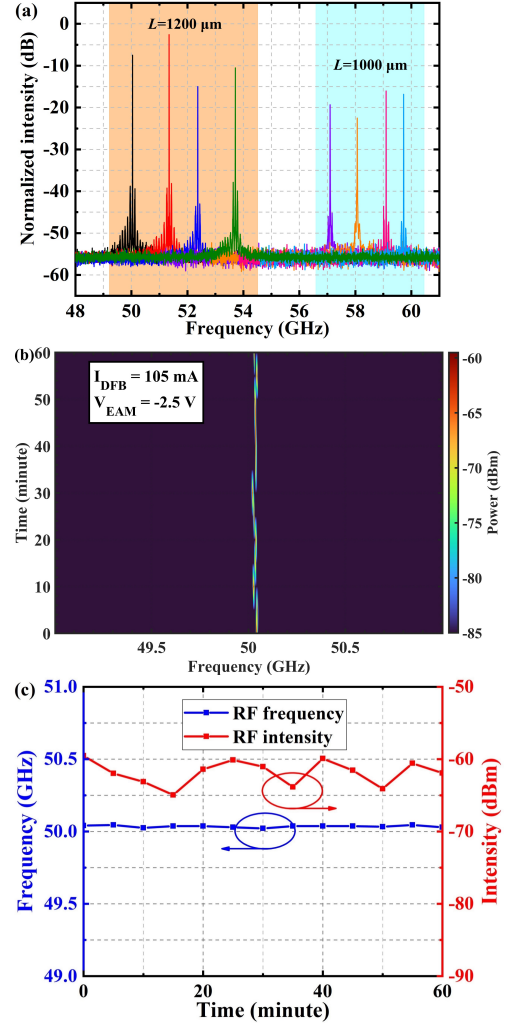**Fig. 12.** Schematic of the RF signal measurement system.

Fig. 13. (a) Measured RF spectrum from laser arrays with different D values for L=1200 μm and 1000 μm, respectively. (b) RF spectral scan over 1 hour at intervals of 5 min for a device with L=1200 μm, D=0.6 μm. (c) RF frequency and intensity versus time.

defined as the mean wavelength between λ_1 and λ_2 ($\lambda_c = (\lambda_1 + \lambda_2)/2$). As shown in Fig. 14, f_s has a variation of –0.063 GHz/nm. According to Fig. 8(a) and (b), the wavelength red shift caused by the current drift is only 0.012 nm/mA, so a change of 11 mA in I_{DFB} will only lead to a 7 MHz frequency shift, which is negligible compared to the smallest RF frequency spacing of 590 MHz of the devices with different L and D.

TABLE III
PARAMETERS OF THE RF SIGNALS FOR DIFFERENT DEVICES

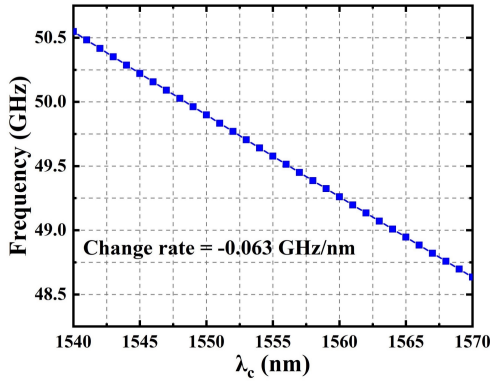| L (μm)	D (μm)	I_{DFB} (mA)	V_{EAM} (V)	f (GHz)	SMSR (dB)
1200	0.60	105	−2.5	50.04	31.3
	0.63	100	−2.1	51.35	35.5
	0.66	103	−2.3	52.37	28.0
	0.69	102	−2.3	53.71	27.3
1000	0.60	112	−1.1	57.11	25.9
	0.63	109	−0.9	58.07	25.3
	0.66	120	−1.4	59.14	27.3
	0.69	118	−1.5	59.73	30.4

Fig. 14. Calculated frequency shift versus λ_c when $\Delta\lambda$ is 0.4 nm.

For the same L, fluctuations in the intensity between the RF signals are caused by the different coupling losses between the lensed fiber and the device in each measurement. It can be seen that the RF signal intensity generated by the devices with L=1000 μm is generally lower than those for L=1200 μm, which is due to the lower PD responsivity at higher frequencies and the lower output power of devices with L=1000 μm.

Through experiments, it was found that RF signals can be obtained under a range of V_{EAM} in one device. The optical linewidth under different V_{EAM} can be obtained by measuring the −20 dB bandwidth of the RF signal [25], and the measured results of a device with L=1200 μm, D=0.6 μm are shown in Fig. 15(a). When taking the measurements, the scanning range of the ESA was 200 MHz, and the resolution bandwidth was 20 kHz. After fitting to a Lorentzian profile, the optical linewidth is equal to the value of the −20 dB bandwidth divided by $2\sqrt{99}$ [25].

As shown in Fig. 15(b), by adjusting V_{EAM}, the maximum and minimum linewidths of 1200-μm-long devices are 280 kHz and 200 kHz respectively. Considering measurement errors, the variation of 80 kHz is considered to be very small, and the typical linewidth of the device under different V_{EAM} remains almost constant. It should be noted that when V_{EAM} is changed from −1.0 V to −1.7 V, over the I_{DFB} range of 0-200 mA, the

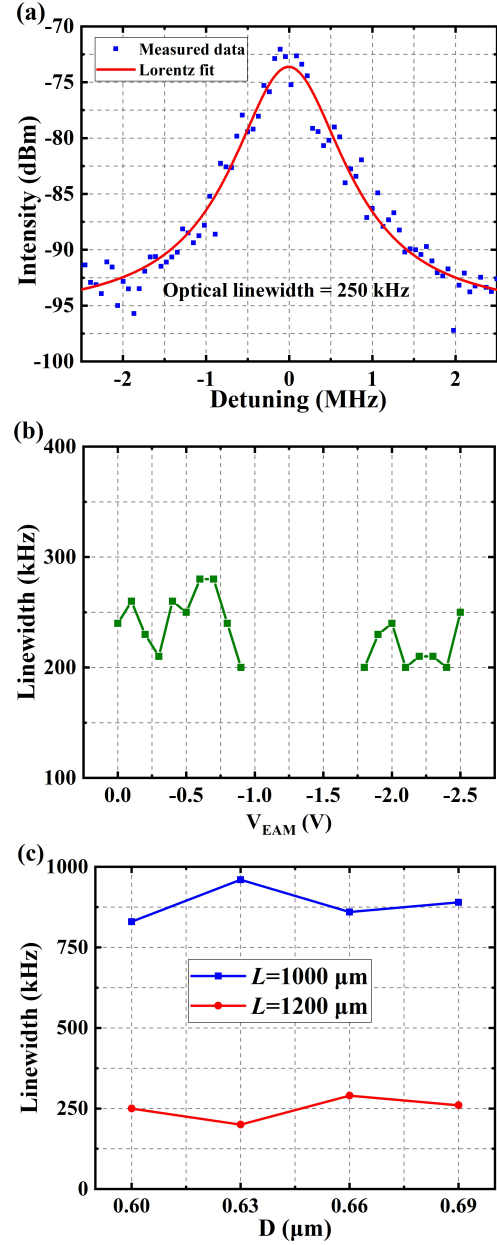**Fig. 15.** (a) RF spectrum of DFB laser with L=1200 μm, 100 MHz scanning range and 20 kHz resolution when I_{DFB}=102 mA, V_{EAM}=−2.5 V. (b) Optical linewidth versus V_{EAM} for a DFB laser with L=1200 μm. (c) Optical linewidth under different L and D.

power difference between the two main modes is larger than 10 dB, and the RF signal cannot be generated by optical beating. As shown in Fig. 15(c), when the L is reduced to 1000 μm, the linewidth of the device increases to around 850 kHz, a change consistent with the description in [26].

IV. CONCLUSION

In this paper, a MDSL array is designed, fabricated and experimentally demonstrated. The κ is modulated to give an inverse-Gaussian distribution along the cavity by changing the alignment of the sidewall grating in each period. Stable dual

wavelength lasing is achieved with a suitable reverse voltage applied to the integrated EAM. Microwave signals, ranging from 50.04 GHz to 59.73 GHz, have been generated by changing the cavity length and grating recess. The experiments show that the typical optical linewidth is 250 kHz and 850 kHz when the cavity length is 1200 μm and 1000 μm, respectively. This is the first report of applying this grating coupling coefficient modulation method to semiconductor DFB lasers and the experimental results prove the device has the potential to be a compact microwave source.

REFERENCES

[1] A. Barh, B. P. Pal, G. P. Agrawal, R. K. Varshney and B. M. A. Rahman, "Specialty Fibers for Terahertz Generation and Transmission: A Review," *IEEE Journal of Selected Topics in Quantum Electronics*, vol. 22, no. 2, pp. 365-379, March-April 2016.

[2] W. Li and J. Yao, "Microwave Generation Based on Optical Domain Microwave Frequency Octupling," *IEEE Photonics Technology Letters*, vol. 22, no. 1, pp. 24-26, Jan.1, 2010.

[3] J. Capmany, D. Novak, "Microwave photonics combines two worlds," *Nature Photonics*, vol. 1, no. 6, pp. 319–330, June 2007.

[4] F. M. A. Al-Zubaidi, J. D. López Cardona, D. S. Montero and C. Vázquez, "Optically Powered Radio-Over-Fiber Systems in Support of 5G Cellular Networks and IoT," *Journal of Lightwave Technology*, vol. 39, no. 13, pp. 4262-4269, July1, 2021.

[5] Pistore, V., Nong, H., Vigneron, PB. *et al.* "Millimeter wave photonics with terahertz semiconductor lasers," *Nature Communication*, vol. 12, pp. 1-7, March 2021.

[6] S. Hisatake, J. -Y. Kim, K. Ajito and T. Nagatsuma, "Self-Heterodyne Spectrometer Using Uni-Traveling-Carrier Photodiodes for Terahertz-Wave Generators and Optoelectronic Mixers," *Journal of Lightwave Technology*, vol. 32, no. 20, pp. 3683-3689, 15 Oct.15, 2014.

[7] U. Gliese *et al.*, "A wideband heterodyne optical phase-locked loop for generation of 3-18 GHz microwave carriers," *IEEE Photonics Technology Letters*, vol. 4, no. 8, pp. 936-938, Aug. 1992.

[8] G. Qi, J. Yao, J. Seregelyi, S. Paquet and C. Belisle, "Optical generation and distribution of continuously tunable millimeter-wave signals using an optical phase modulator," *Journal of Lightwave Technology*, vol. 23, no. 9, pp. 2687-2695, Sept. 2005.

[9] J. Liu *et al.*, "Efficient Optical Millimeter-Wave Generation Using a Frequency-Tripling Fabry–Pérot Laser with Sideband Injection and Synchronization," *IEEE Photonics Technology Letters*, vol. 23, no. 18, pp. 1325-1327, Sept.15, 2011.

[10] J. Sun, Y. Dai, X. Chen, Y. Zhang and S. Xie, "Stable Dual-Wavelength DFB Fiber Laser With Separate Resonant Cavities and Its Application in Tunable Microwave Generation," *IEEE Photonics Technology Letters*, vol. 18, no. 24, pp. 2587-2589, Dec.15, 2006.

[11] Y. Zhang *et al.*, "A Stable Dual-Wavelength DFB Semiconductor Laser With Equivalent Chirped Sampled Grating," *IEEE Journal of Quantum Electronics*, vol. 58, no. 1, pp. 1-7, Feb. 2022

[12] L. Hou, M. Haji, I. Eddie, H. Zhu, and J. H. Marsh, "Laterally coupled dual-grating distributed feedback lasers for generating mode-beat terahertz signals," *Opt. Lett*. vol. 40, pp. 182-185, 2015

[13] F. Pozzi, R. M. De La Rue and M. Sorel, "Dual-Wavelength InAlGaAs–InP Laterally Coupled Distributed Feedback Laser," *IEEE Photonics Technology Letters*, vol. 18, no. 24, pp. 2563-2565, Dec.15, 2006.

[14] M. Takashi, H. Kawaguchi, "Characteristics of nondegenerate four-wave mixing in electroabsorption modulator, " *Applied Physics Letters*, vol. *85*, no. 6, pp.869-871 2004.

[15] X. Wang *et al.*, "Precise control of the coupling coefficient through destructive interference in silicon waveguide Bragg gratings," *Opt. Lett*. vol 39, pp. 5519-5522, 2014.

[16] B. Lin, *et al.*, "Analysis of inverse-Gaussian apodized fiber Bragg grating," *Appl. Opt.* vol. 49, no. 25, pp. 4715-4722, 2010.

[17] Bo Lin, S. Tjin, M. Jiang, and P. Shum, "Tunable microwave generation based on a dual-wavelength fiber laser with an inverse-Gaussian apodized fiber Bragg grating," *Appl. Opt.* vol. 50, no. 25, pp. 4912-4916, 2011.

[18] T. Erdogan, "Fiber grating spectra," *Journal of Lightwave Technology*, vol. 15, no. 8, pp. 1277-1294, Aug. 1997.

[19] G. P. Agrawal and N. K. Dutta, *Long-Wavelength Semiconductor Lasers*, New York: Van Nostrand, 1968, pp. 305–305.

[20] R. Chanson *et al.*, "Global Model of Cl$_2$/Ar High-Density Plasma Discharge and 2-D Monte-Carlo Etching Model of InP," *IEEE Transactions on Plasma Science*, vol. 40, no. 4, pp. 959-971, April 2012.

[21] P. Strasser, R. Wuest, F. Robin, D. Erni and H. Jackel, "Process optimization for dry etching of InP-InGaAsP-based photonic crystals with a Cl$_2$/CH$_4$/H$_2$ mixture on an ICP-RIE," *16th IPRM. 2004 International Conference on Indium Phosphide and Related Materials, 2004.*, 2004, pp. 175-178.

[22] K. A. Winick, "Longitudinal mode competition in chirped grating distributed feedback lasers," *IEEE Journal of Quantum Electronics*, vol. 35, no. 10, pp. 1402-1411, Oct. 1999.

[23] L. Hou *et al.*, "Subpicosecond Pulse Generation at Quasi-40-GHz Using a Passively Mode-Locked AlGaInAs–InP 1.55- μm Strained Quantum-Well Laser," *IEEE Photonics Technology Letters*, vol. 21, no. 23, pp. 1731-1733, Dec.1, 2009.

[24] S. K. C. Liew, "Above-threshold analysis of loss-coupled DFB lasers: threshold current and power efficiency," *IEEE Photonics Technology Letters*, vol. 7, no. 12, pp. 1400-1402, Dec. 1995.

[25] Zhongan Zhao, Zhenxu Bai, Duo Jin, Yaoyao Qi, Jie Ding, Bingzheng Yan, Yulei Wang, Zhiwei Lu, and Richard P. Mildren, "Narrow laser-linewidth measurement using short delay self-heterodyne interferometry," *Opt. Express*, vol. 30, pp.30600-30610, 2022.

[26] H. Ishii, K. Kasaya and H. Oohashi, "Spectral Linewidth Reduction in Widely Wavelength Tunable DFB Laser Array," *IEEE Journal of Selected Topics in Quantum Electronics*, vol. 15, no. 3, pp. 514-520, May-June, 2009.

Bocheng Yuan received the B.S. and master's degrees from the College of Electronic and Optical Engineering and the College of Microelectronics, Nanjing University of Posts and Telecommunications, Nanjing, Jiangsu, China, in 2018 and 2021, respectively. He is now pursuing his Ph.D. in James Watt School of Engineering, University of Glasgow. His research fields include DFB semiconductor lasers and photon integrated circuits.

Yizhe Fan was born in Hangzhou, China. He received the Bachelor's degree from University of Electronic Science and Technology of China in 2021. He is currently pursuing the Ph.D. from University of Glasgow. His current research interests are in semiconductor DFB laser and nanofabrication.

Shengwei Ye Shengwei Ye was born in Wuhan, Hubei, China. He received the B.S. degree in the year of 2011, from the School of Science, Hubei University of Technology, and received his Doctoral degree in the year of 2018, from the School of Optoelectronic Information, University of Electronic Science and Technology of China, Chengdu, China. Since the year of 2018, he works at University of Glasgow as a research assistant. His research interests include silicon-based graphene optoelectronics devices, III-V materials based DFB laser devices and uni-traveling carrier photodiodes.

Yunshan Zhang received the B.S. degree in science and technology of electronics from Shandong University, Jinan, China, in 2002, and the Ph.D. degree in physical electronics from the Beijing Institute of Technology, Beijing, China, 2011. He is currently a Postdoctor with the College of Engineering and Applied Sciences, Nanjing University, Nanjing, China. His research interests include solid state lasers, DFB semiconductor lasers, fiber communication, and photonic integrated circuits. He is also majoring in design of DFB lasers and laser arrays.

Yimin Sun was born in Hunan, China. He received the B.E. degree from the Bangor University and the M.A. degree from the University of Sheffield. He is currently pursuing the Ph.D. at University of Glasgow. His research interests include optical communications, DFB lasers, laser arrays, and photonic integrated circuits.

Xiao Sun received the B.Eng. degree in Electrical and Electronic Engineering from University of Electronic Science and Technology of China. He is currently working toward the Ph.D. degree in Electrical and Electronic Engineering with James Watt School of Engineering, University of Glasgow. His research interests include photonic integrated circuits and nanofabrication.

Weiqing Cheng was born in Changchun, China, in 1997. She received the B.E. degree in Electrical and Electronic Engineering from University of Electronic Science and Technology of China, Chengdu, China, in 2020. She started her Ph.D. project in the Photonic Integrated Circuit research group at the University of Glasgow in 2020. She has been engaged in research on high sensitivity microring biochemical sensors based on SOI platform, surface plasmonic resonance based on metal/dielectric interface, and semiconductor ring-resonator-coupled tunable laser.

Song Liang was born in Liaoning, China, in 1976. He received the B.S. and M.S. degrees from the Department of Material Physics, Beijing University of Science and Technology, Beijing, China, in 1999 and 2002, respectively, and the Ph.D. degree from the Institute of Semiconductor, Chinese Academy of Sciences, Beijing, in 2006. He is currently a Professor with the Institute of Semiconductors, Chinese Academy of Sciences. His current research interests include the MOCVD growth of semiconductor materials and the fabrication of related optoelectronics devices.

Yongguang Huang was born in Fujian, China, in 1981. He received the B.S. degree from the Minzu University of China in 2004, and the Ph.D. degree from the Beijing University of Technology in 2010. He works as an Associate Professor at the Key Laboratory of Semiconductor Materials Science, Institute of Semiconductors, Chinese Academy of Sciences. He has ever been a Visiting Scholar at Aston University, U.K. His current research includes high-speed DFB laser chips, high power semiconductor lasers, and photonic integrated circuits.

Ruikang Zhang received the M.Sc. degree in physics from Wuhan University, Wuhan China, in 1999 and the Ph.D. degree in electrical engineering from the Beijing University of Posts and telecommunications, Beijing, China, in 2002. Since 2011 he worked at the Institute of Semiconductors, Chinese Academy of Sciences. His current research interests include the optimization of high-speed semiconductor devices, optoelectronic devices, and photonic integrated circuits.

Jue Wang received the PhD degree in Electronics and Electrical Engineering from the University of Glasgow in 2014. He has been working on THz device technology including high power sources and high-sensitive detectors based on resonant tunnelling diode. His research also focuses on terahertz applications including ultrafast wireless communications and THz imaging.

John H. Marsh (M'91–SM'91–F'00) received the B.A. degree from the University of Cambridge, Cambridge, U.K., the M.Eng. degree from the University of Liverpool, Liverpool, U.K., and the Ph.D. degree from the University of Sheffield, Sheffield, U.K. He is currently Professor of Optoelectronic Systems with the University of Glasgow, Glasgow, U.K. He co-founded Intense Ltd. in 2000. His research interests include fundamental electrical and optical properties of semiconductors, development of novel optoelectronic devices, processes for creating photonic integrated circuits, integrated mode-locked lasers for ultrashort pulse generation, and the development and manufacturing of high-power laser array products. He is a Fellow of Royal Academy of Engineering, Royal Society of Edinburgh, Optica, IET, Institute of Physics, and Royal Society of Arts. He was the recipient of the 2006 IEEE/LEOS Engineering Achievement Award with Catrina Bryce "for extensive development and commercialization of quantum well intermixing for photonic devices." He was also awarded the 2006 IEEE/LEOS Distinguished Service Award "for major contributions to LEOS governance and for leadership in promoting the development of LEOS as a global society." He was President of the IEEE Photonics Society in 2008 and 2009.

Lianping Hou (M'11-SM'18) received the B.Eng. degree from the Central-South University of Technology, Changsha, China, in 1992, the M.A. degree from Huazhong University of Science and Technology, Wuhan, China, in 2003, and the Ph.D. degree from the Chinese Academy of Sciences, Beijing, China, in 2005. In 2006, he was with the Department of Electrical and Electronic Engineering, University of Bristol, as a Research Associate. In 2007, he was with the School of Engineering, University of Glasgow, as a Research Associate. In 2016, he was promoted to lecturer. He is currently a Reader at the University of Glasgow, Glasgow, U.K., working on nanofabrication, semiconductor laser technology, integrated optics, terahertz Technology, and optical biosensors. He is the author and co-author of more than 170 papers and the inventor of several patents.